Available online at www.sciencedirect.com
ScienceDirect
European Journal of Mechanics B/Fluids 26 (2007) 688–705

Investigation of a re-entrant jet reflection at an inclined cavity closure line

Matevž Dular [a,*], Rudolf Bachert [b], Christian Schaad [b], Bernd Stoffel [b]

[a] *Laboratory for Water and Turbine Machines, University of Ljubljana, Askerceva 6, 1000 Ljubljana, Slovenia*
[b] *Laboratory for Turbomachinery and Fluid Power, Darmstadt University of Technology, Magdalenenstr. 4, 64289 Darmstadt, Germany*

Received 18 July 2006; received in revised form 8 January 2007; accepted 9 January 2007

Available online 20 January 2007

Abstract

Cavitation on two-dimensional hydrofoils with swept leading edges always displays some 3-dimensional effects. It is well known that the cavity closure on such hydrofoil is not perpendicular to the channel walls, but is curved in a distinctive pattern. The cavitation pocket is longer in the region where the hydrofoil is the shortest. Also the dynamics of cavitation is very distinctive. In the region where the hydrofoil is the longest attached and steady cavitation with no cloud separation exists. On the other side, where the hydrofoil is the shortest, cavitation cloud separations occur.

Different explanations for this pattern were proposed in the past but they have not jet been clearly confirmed neither experimentally nor by numerical simulation.

In the present paper a clear explanation supported by the numerical simulation and also by experimental measurements, is given.

Keywords: Cavitation; Swept leading edge; CFD; PIV-LIV method; Re-entrant jet reflection

1. Introduction

It is well known that the cavity closure on a two-dimensional hydrofoil with swept leading edge is not perpendicular to the channel walls, but is curved in a distinctive pattern (de Lange and de Bruin [1]). The cavitation pocket is longer in the region where the hydrofoil is the shortest. Also the dynamics of cavitation is very distinctive. In the region where the hydrofoil is the longest attached and steady cavitation with no cloud separation exists. On the other side, where the hydrofoil is the shortest, cavitation cloud separations occur (Fig. 1).

Different explanations for this pattern were proposed. It seems that de Lange and de Bruin [1] and Duttweiler and Brennen [2] gave the most plausible explanation.

The re-entrant jet velocity gains a spanwise component if the closure line of the cavity is inclined. Assuming that the pressure gradient has no component along the closure line, the conservation of the tangential momentum implies

* Corresponding author. Tel.: +386 1 4771 453; fax: + 386 1 2518 567.
E-mail addresses: matevz.dular@fs.uni-lj.si, matevz.dular@email.si (M. Dular), bachertr@auma.com (R. Bachert), schaad@tfa.maschinenbau.tu-darmstadt.de (C. Schaad), stoffel@tfa.maschinenbau.tu-darmstadt.de (B. Stoffel).

0997-7546/$ – see front matter
doi:10.1016/j.euromechflu.2007.01.001

Nomenclature

C_c	constant in the vapour condensation term expression	R_c	vapour condensation source term ... kg/m^3 s
C_e	constant in the vapour generation term expression	u_m	mixture velocity ... m/s
$C_{1\varepsilon}$	coefficient	v	flow velocity ... m/s
$C^*_{2\varepsilon}$	coefficient	α_k	inverse effective turbulent Prandtl number
f_g	gas mass fraction	α_ε	inverse effective turbulent Prandtl number
f_v	vapour mass fraction	ε	turbulence dissipation rate ... m^2/s^3
k	turbulence kinetic energy ... m^2/s^2	γ	liquid surface tension ... N/m
n	exponent	μ_{eff}	effective viscosity ($\mu + \mu_t$) ... Pa s
p	pressure ... Pa	μ_m	mixture viscosity ... Pa s
p_{ref}	reference pressure ... Pa	μ_t	turbulent viscosity ... Pa s
p_v	vapour pressure ... Pa	ρ	density ... kg/m^3
P_k	generation of turbulent kinetic energy ... kg/m s^3	ρ_l	liquid density ... kg/m^3
		ρ_m	mixture density ... kg/m^3
		ρ_v	vapour density ... kg/m^3
R_e	vapour generation source term ... kg/m^3 s	σ	cavitation number

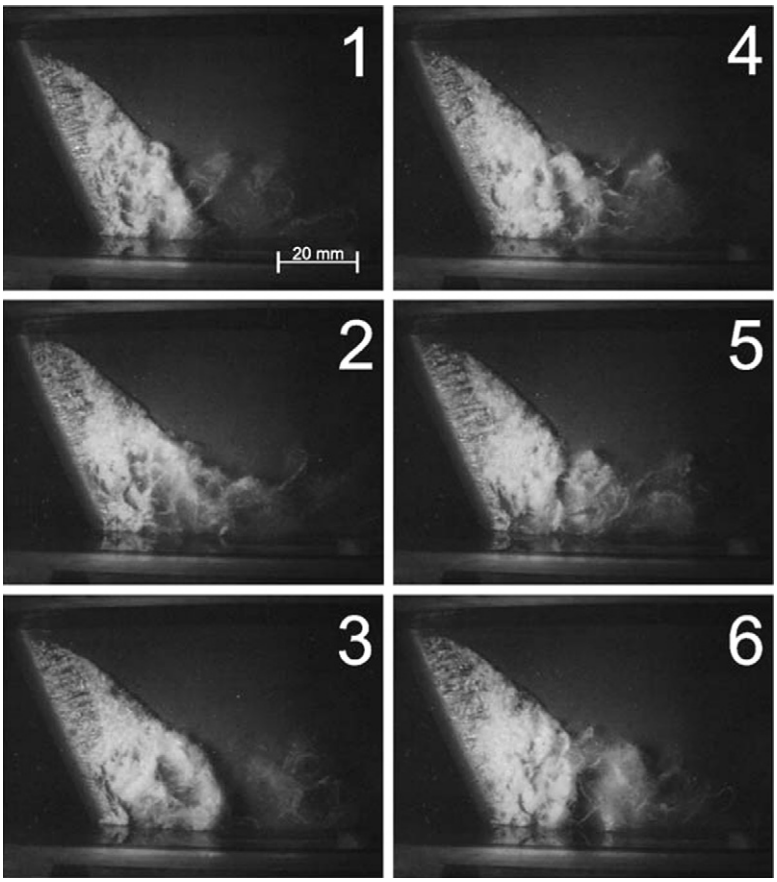

Fig. 1. Sequence showing asymmetrical cavitation cloud behaviour of a swept leading edge hydrofoil that was used in the present study (flow is from left to right).

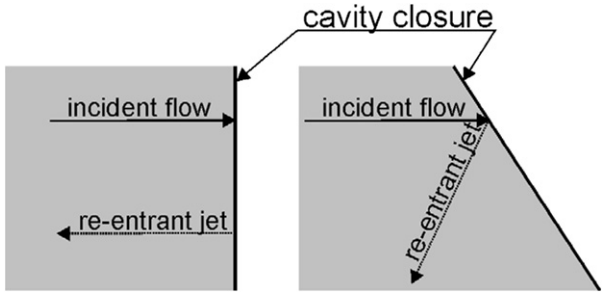

Fig. 2. Reflection of the incident flow by the cavity closure line (Lange and de Bruin [1]) – the flow is from left to right.

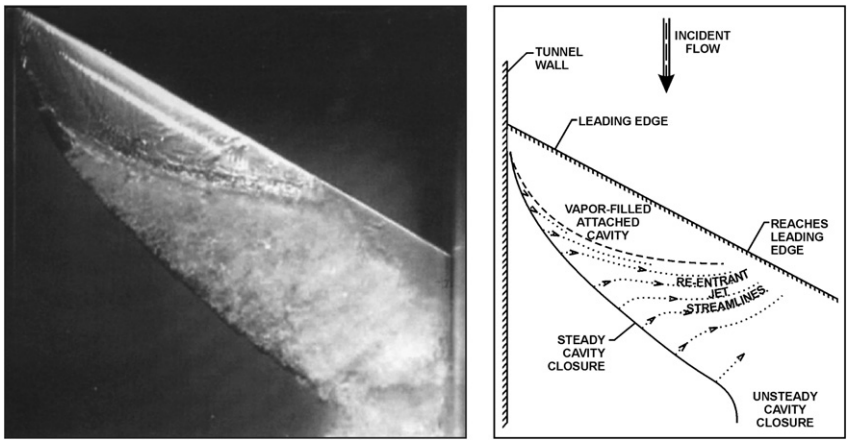

Fig. 3. Cavitation on a swept leading edge hydrofoil (Laberteaux and Ceccio [3]) and interpretation of the effect (Duttweiler and Brennen [2]) – the flow is from top to bottom.

that the velocity component tangential to the cavity closure line remains unchanged. It results that the incident velocity is simply reflected at the cavity closure line Fig. 2. In fact this mirror-like reflection idea is only valid for a simplified two-dimensional steady flow case, but it is nevertheless useful for simple interpretation of the phenomenon.

The first interpretation of the actual effect was done on the base of visual observation of cavitating hydrofoil (Laberteaux and Ceccio [3]) – experiment and Duttweiler and Brennen [2] – interpretation) (Fig. 3). Two very different regions in the cavity interface are clearly visible. In the region where the hydrofoil is the longest the cavity is glossy and steady, whereas the other side it is frothy and unsteady. The presumed re-entrant jet flow can also be divided into two parts. In the region where the hydrofoil is the longest the closure line is very inclined, the re-entrant jet never reaches the leading edge and thus delimits a vapour-filled cavity, whereas in the region where the hydrofoil is the shortest, the cavity closure line is less inclined, the re-entrant jet, by impinging on the cavity interface, generates a liquid-vapour mixture and unsteady cavitation.

The abovementioned hypothesis bases only on visual observation of vapour pockets and has been confirmed neither experimentally (actual velocity measurements) nor numerically.

In the present paper the results of numerical simulation and also of velocity measurements, that confirm the abovementioned hypothesis, are presented.

In the last decade various methods for numerical simulation of cavitating flow were developed. Most of the studies treat the two phase flow as a single vapour–liquid phase mixture flow. The evaporation and condensation can be modeled with different source terms that are usually derived from the Rayleigh–Plesset bubble dynamics equation. Different authors proposed to consider a transport equation model for the void ratio, with vaporization/condensation source terms to control the mass transfer between the two phases (Kubota [4], Kunz et al. [5], Senocak and Shyy [6], Singhal et al. [7] and Owis and Nayfeh [8]). The commercial CFD code Fluent 6.1.18 was used for 3D simulations of cavitating flow around a hydrofoil with swept leading edge. A transient simulation was performed to simulate the unsteady behaviour of cavitation including the shedding of vapour structures. Numerical model uses an implicit

finite volume scheme, based on a SIMPLE algorithm, associated with multiphase and cavitation model, based on a simplified Rayleigh–Plesset equation for bubble dynamics (Singhal et al. [7]). This method has the advantage that it can take into account the time influence on the mass transfer phenomena through empirical laws for the source term. It also avoids using, hard to determine, quantities like bubble number density and initial bubble diameter. A RNG k–ε turbulence model with a modified turbulent viscosity term was used. Results of previous studies (Dular et al. [9]) showed that the method that was used accurately predicts many features of developed cavitating flow including the cavitation cloud separation, pressure distribution, re-entrant jet formation, shedding frequency and also – most importantly for the present study – the influence of the swept leading edge.

Many techniques to determine the velocity distribution in cavitating flow exist. Laberteaux and Ceccio [3] upgraded the PIV (particle image velocimetry) technique of Zhang et al. [10] to measure velocities in a developed cavitating flow with vapour cloud separation. However they were unable to obtain the information about the velocity field inside the cavitation itself. The problem they faced was overexposure of the particles added to the water (they were not visible since the vapour structure reflects much more light), so the velocity field inside the cavitation structure was not determined. The method applied in the present study, which allows also the flow measurements inside the vapour structure and the simultaneous acquisition of the shape of the cavitation structure, is a combination of PIV method, LIF (Laser Induced Fluorescence) technique and a use of two cameras (Dular et al. [9], Bachert et al. [11] and Friedrichs and Kosyna [12]). Velocity distribution on a plane 1 mm above the hydrofoil surface was evaluated and interpreted for the present study.

The paper describes a numerical simulation and PIV-LIF measurements of the cavitating flow around the hydrofoil. From the acquired results conclusions about the hypothesis of the swept leading edge influence on the flow by de Lange and de Bruin [1] and Duttweiler and Brennen [2] were drawn.

Numerical and experimental methods that were used for the present study are only briefly presented here, since they were already described in detail in the previous paper by the present authors (Dular et al. [9]), where also an extensive evaluation of the simulation was shown.

2. Experimental set-up

2.1. The hydrofoil and the cavitation tunnel

Experiments were set up in a cavitation tunnel at the Laboratory for Turbomachinery and Fluid Power – Darmstadt University of Technology. A simple 50 mm wide, 107.9 mm long and 16 mm thick symmetric hydrofoil with circular leading edge and parallel walls was used. In order to obtain three-dimensional cavitation effects the basic geometry was modified by sweeping back the leading edge at an angle of 25° degrees (Fig. 4).

The hydrofoil was inserted into the rectangular test section of a cavitation tunnel with closed circuit that enabled to change the system pressure and consequently the cavitation number. The test section is 500 mm long, 100 mm high and 50 mm wide. The velocity in the reference plane upstream of the hydrofoil was held constant at 13 m/s ($Re = 1.38 \times 10^6$). The turbulence intensity level upstream of the hydrofoil was derived from the LDA measurements

Fig. 4. Simple hydrofoil with a swept leading edge.

and was 3% (Dular et al. [9]). The measurement of flow velocity was made with inductive flow meter Fischer and Porter D10D with an uncertainty of 1% of the measured value.

Developed cavitating flow was observed at an incidence angle of 5° and at cavitation number of 2.3, which is defined as the difference between system and vapour pressure (at system temperature) divided by the dynamic pressure:

$$\sigma = \frac{p_{\mathrm{ref}} - p_{\mathrm{v}}}{\rho v^2/2}. \tag{1}$$

The system pressure was measured with sensor JPB – Type 304 on each channel wall, 5 chord lengths upstream of the hydrofoil and then averaged. The fluid temperature was measured with Jumo PT100 sensor. Considering the combination of inaccuracies of pressure, velocity and temperature measurements, the cavitation number could be determined within ±0.04 of the measured value (Hofmann et al. [13]).

The water used for the experiments was almost saturated with gasses (more then 50 mg of gas per liter of water) so that the effects of the tensile strength were reduced to the minimum possible level. This condition is necessary since the variations in water quality can greatly influence the cavitation behaviour as reported by Iwai and Li [14].

2.2. PIV-LIF measurements

The combination of the PIV technique with LIF technique makes it possible to obtain the information about the velocity field outside and inside the cavitation pocket on the hydrofoil. A technique of combining the PIV method with the LIF technique to obtain the information on the velocity field outside and inside the vapour structure was used together with two CCD-cameras (Fig. 5) so that the location and extent of the instantaneous vapour zones was determined simultaneously with the corresponding velocity field (Dular et al. [9]), Bachert et al. [11] and Friedrichs and Kosyna [12]).

Two CCD-cameras were installed with their optical axes oriented orthogonally to the light sheet. Special fluorescent tracer particles (PMMA-Rhodamine B, diameter is 1–20 μm) were added to the water for the PIV measurements. The particles receive light from the laser at a wavelength of 532 nm (green spectrum) and emit light at a wavelength of 590 nm (yellow spectrum). By fitting one of the two CCD-cameras with an appropriate light filter (that filters the visible light but lets the light in yellow spectrum trough) it is possible to get suitable images of the tracer particles for the PIV analysis with the PIV-camera (the one with the filter) while the second camera takes an image in the whole spectrum of light and records the visible cavitation structure at the same time. Since one camera records only the light in the yellow spectrum, the cavitation structure is filtered out of that image and tracer particles inside it can also be detected. A raw image captured by Camera 1 where only particles are visible is presented in Fig. 6 (the flow is from top to bottom).

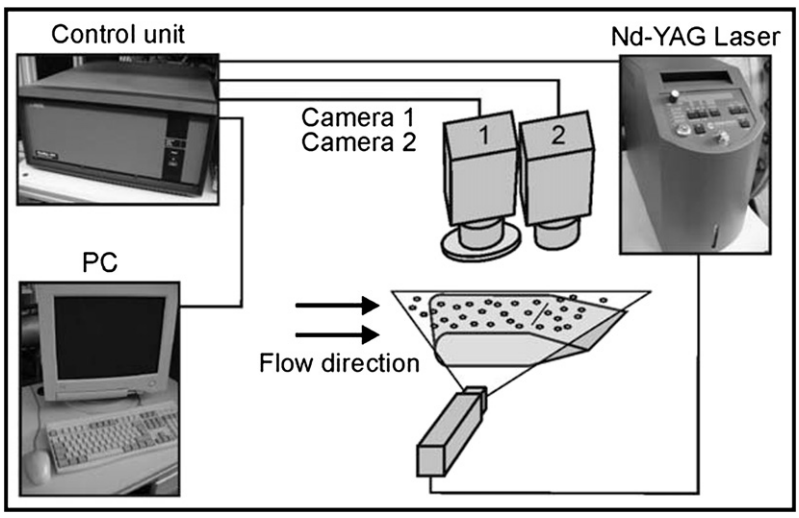

Fig. 5. Experimental set-up.

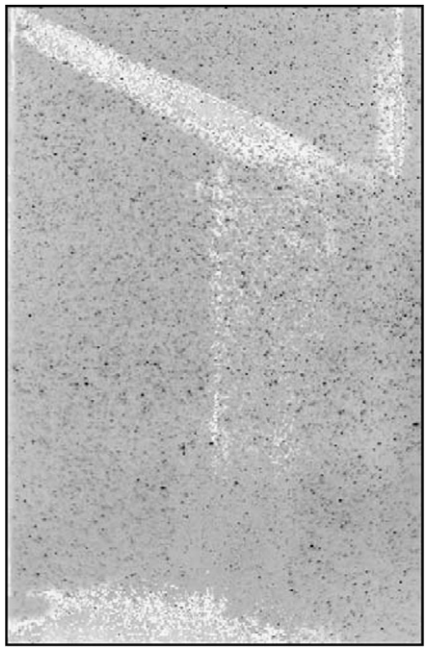

Fig. 6. Raw image of tracer particles above the hydrofoil.

The region of interest was illuminated by a 1 mm thick laser light-sheet (Nd-YAG-Laser) that was parallel to the surface of the hydrofoil. The thickness of the re-entrant jet was first estimated from the results of measurements of the velocities in the plane perpendicular to the hydrofoils surface (Dular et al. [9]). A maximum thickness of approximately 1.5 mm was determined, what also agrees with the results of present numerical simulation. Nevertheless, we positioned the light sheet at various distances from the hydrofoil surface (0.5, 1, 2 and 4 mm) to determine the best compromise between the sufficient data rate and the acquisition of the re-entrant jet (Fig. 7).

In Fig. 7 shows instantaneous situations where conventional images of cavitation structures and the corresponding velocity fields at various distances from the hydrofoil surface are presented.

When observing the velocity fields for the cases of 0.5 and 1 mm distance one can see an evident backflow, re-entrant jet, in the region between the leading edge of the hydrofoil and the cavity closure. This kind of flow (flow in the direction from the cavity closure towards the leading edge) cannot be seen on planes 2 and 4 mm from the hydrofoil surface, where a somewhat distorted velocity field with no clear direction was captured (the majority of the vectors point toward in the incipient flow direction). This implies that the thickness of the jet is in fact in the order of 1 to 2 mm.

On the other hand, in the case of distance of 0.5 mm, problems with sufficient data rate occurred and results were not reliable any more (one can see many vectors that deviate significantly from their neighbor vectors – bad vector percentage was high).

It was concluded, on the basis of the these studies, that the laser light sheet should be positioned at a distance of 1 mm from the hydrofoil surface for optimal acquisition of the re-entrant jet flow at a sufficient data rate.

The two cameras were triggered by the control unit of the PIV-system in combination with the laser shots with duration of 10 ns. For the PIV analyses 2 images with 30 μs time delay were recorded. Using the standard DANTEC software a cross correlation of the two images of tracer particles was made. The image size was 1152×858 pixel, equal to 98.8×78.8 mm (8.6×10^{-2} mm/Pixel in x-direction and 9.2×10^{-2} mm/Pixel in y-direction). A low-pass Gaussian sub-pixel interpolation was used for the determination of the correlation peak. The size of the interrogation area was 16×16 pixels; a local shift was applied so that the overleaping was 50% what lead to a distance of approximately 0.7 mm between the vectors. About 20% of all vectors were rejected in the area where no flow is present (for example the part of the image where only the channel walls can be seen). Additionally about 2% of the remaining vectors were recognized as invalid "bad" vectors (a bad vector was defined as a vector exceeding a threshold stan-

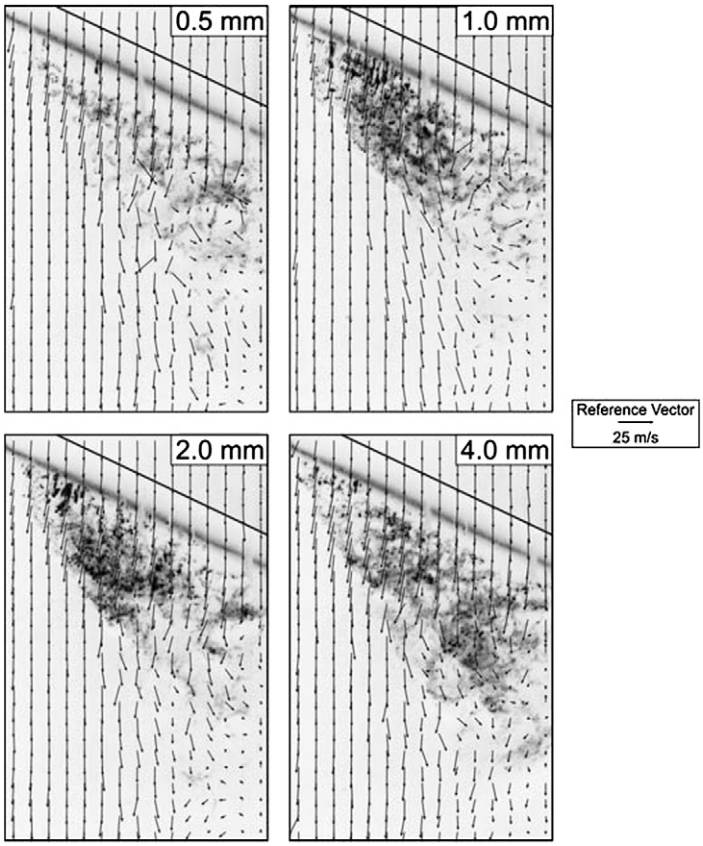

Fig. 7. Measured instantaneous velocity fields with corresponding cavitation structures at different distances from the hydrofoil surface.

dard deviation from its nearest neighbors) and were substituted by the average of their nearest neighbors. The field was then smoothed by a Gaussian weighted averaging technique. The average uncertainty of measured velocity using PIV-LIF technique was estimated to 2% (Dular et al. [9]). The images of both cameras were recorded simultaneously. The result of the PIV analysis (vectorplot) can be then superposed to the conventional image of the cavitating zone taken by the second camera to be able to present the information on the magnitude and the direction of the flow velocity and on the location, size and shape of the corresponding cavitation structure in one figure. Image capturing frequency (0.5 Hz) was much lower that the frequency of the phenomena (over 300 Hz as it will be later pointed out) so we were not able to get the time evolution of the velocity field. However we were able to construct a probable sequence of events (Fig. 14) on the basis of comparing single images (PIV-LIF data) to the high-speed camera movies (Bachert [15]).

A more detailed description of the experimental technique that was used can be found in the previous paper by the present authors (Dular et al. [9]).

3. Numerical simulation

A program package Fluent 6.1.18 was used to calculate the cavitating flow. It is a 3-dimensional structured mesh code that solves a set of time dependent Reynolds-averaged Navier–Stokes equations (URANS) in a conservative form. The numerical model uses an implicit finite volume scheme, based on a SIMPLE algorithm (Patankar [16]), associated with multiphase and cavitation model. The SIMPLE algorithm needs to be modified in a similar way as for the case of highly compressible flows (Senocak and Shyy [6]). A 2nd order implicit temporal discretization was used. A 2nd order upwind differentiating scheme was used. A relatively high under-relaxation factor for the volume fraction (0.25), which does not influence the final solution but still allows a stable simulation, was used.

3.1. Basic multiphase model

A single fluid (mixture phase) approach was used. The basic approach consists of using the standard Reynolds averaged Navier–Stokes viscous flow equations and a conventional turbulence model (RNG k–ε model). The mass (Eq. (4)) and momentum (Eq. (5)) conservation equations together with the transport equation (Eq. (6)) and the equations of the turbulence model (Eqs. (9) and (10)) form the set of equations from which the fluid density (which is a function of vapour mass fraction f_v) is computed. The $\rho_\mathrm{m} - f_\mathrm{v}$ (mixture density – vapour mass fraction) relationship is:

$$\frac{1}{\rho_\mathrm{m}} = \frac{f_\mathrm{v}}{\rho_\mathrm{v}} + \frac{1 - f_\mathrm{v}}{\rho_\mathrm{l}}. \tag{2}$$

The volume fraction of the vapour phase (α_v) is related to of the mass fraction of the vapour phase with:

$$\alpha_\mathrm{v} = f_\mathrm{v} \frac{\rho_\mathrm{m}}{\rho_\mathrm{v}}. \tag{3}$$

The mass conservation equation for the mixture is:

$$\frac{\partial \rho_\mathrm{m}}{\partial t} + \frac{\partial (\rho_\mathrm{m} \bar{u}_{\mathrm{m},j})}{x_j} = 0. \tag{4}$$

The momentum conservation equation for the mixture reads:

$$\frac{\partial (\rho_\mathrm{m} \bar{u}_{\mathrm{m},i})}{\partial t} + \frac{\partial (\rho_\mathrm{m} \bar{u}_{\mathrm{m},j} \bar{u}_{\mathrm{m},i})}{\partial x_j} = -\frac{\partial \bar{p}}{\partial x_i} + \frac{\partial}{\partial x_j}\left[\mu_\mathrm{m}\left(\frac{\partial \bar{u}_{\mathrm{m},i}}{\partial x_j} + \frac{\partial \bar{u}_{\mathrm{m},j}}{\partial x_i}\right) - \rho_\mathrm{m}\overline{u'_{\mathrm{m},i} u'_{\mathrm{m},j}}\right], \tag{5}$$

and the transport equation for the vapour is given by:

$$\frac{\partial (\rho_\mathrm{m} f_\mathrm{v})}{\partial t} + \frac{\partial (\rho_\mathrm{m} \bar{u}_{\mathrm{m},j} f_\mathrm{v})}{\partial x_j} = R_\mathrm{e} - R_\mathrm{c}, \tag{6}$$

where R_e and R_c are the source terms that are described in the next section.

3.2. Cavitation model

Source terms R_e and R_c that are included in the transport equation define vapour generation (liquid evaporation) and vapour condensation, respectively. Source terms are functions of local flow conditions (static pressure, velocity) and fluid properties (liquid and vapour phase densities, saturation pressure and liquid surface tension). The source terms are derived from the Rayleigh–Plesset equation, where high order terms and viscosity term have been left out. The derivation of the source terms can be found in Singhal et al. [7].

They are given by:

$$R_\mathrm{e} = C_\mathrm{e} \frac{\sqrt{k}}{\gamma} \rho_\mathrm{l} \rho_\mathrm{v} \sqrt{\frac{2}{3} \frac{p_\mathrm{v} - p}{\rho_\mathrm{l}}} (1 - f_\mathrm{v} - f_\mathrm{g}), \tag{7}$$

when $p_\mathrm{v} > p$, and by:

$$R_\mathrm{c} = C_\mathrm{c} \frac{\sqrt{k}}{\gamma} \rho_\mathrm{l} \rho_\mathrm{l} \sqrt{\frac{2}{3} \frac{p - p_\mathrm{v}}{\rho_\mathrm{l}}} f_\mathrm{v}, \tag{8}$$

when $p_\mathrm{v} < p$, where C_e and C_c are empirical constants, k is the local kinetic energy, γ surface tension, f_v vapour mass fraction and f_g mass fraction of noncondensable (dissolved) gases. C_e and C_c were determined by Singhal et al. [7] by comparing experimental and numerical results at different combinations of initial conditions and geometries; their values are 0.02 and 0.01, respectively.

3.3. Turbulence model

For the present case a two-equation k–ε RNG turbulence model by Yakhot and Orszag [17] was applied. Additional equations that were used to close the system of equations are:

$$\frac{\partial(\rho k)}{\partial t} + \frac{\partial(\rho k \bar{u}_j)}{\partial x_j} = \frac{\partial}{\partial x_j}\left[\alpha_k \mu_{\text{eff}} \frac{\partial k}{\partial x_j}\right] + P_k - \rho\varepsilon \tag{9}$$

and

$$\frac{\partial(\rho \varepsilon)}{\partial t} + \frac{\partial(\rho \varepsilon \bar{u}_j)}{\partial x_j} = \frac{\partial}{\partial x_j}\left[\alpha_\varepsilon \mu_{\text{eff}} \frac{\partial \varepsilon}{\partial x_j}\right] + C_{1\varepsilon}\frac{\varepsilon}{k} P_k - C^*_{2\varepsilon}\rho\frac{\varepsilon^2}{k}. \tag{10}$$

The RNG k–ε turbulence model was applied for solving the transport equations of the turbulent kinetic energy and its dissipation rate. The model itself is unable to correctly simulate the unsteady behaviour of cavitation. After an initial fluctuation of the cavity volume, the calculation leads to a quasi-steady behaviour of the cavitation sheet, which becomes stable. Also the overall length of the predicted cavity structure is about 50% too short compared to experimental results. To improve the simulation a modification of the turbulent viscosity was applied as it was proposed and successfully proven by Reboud et al. [18]. In regions with higher vapour volume fractions (lower mixture densities) a modification of the RNG k–ε turbulence model was made by artificially reducing the turbulent viscosity of the mixture:

$$\mu_t = f(\rho) C_\mu \frac{k^2}{\varepsilon}, \tag{11}$$

$$f(\rho) = \rho_v + \frac{(\rho_m - \rho_v)^n}{(\rho_l - \rho_v)^{n-1}} \quad \text{where } n \gg 1. \tag{12}$$

This modification limits the turbulent viscosity in the region filled mainly by vapour phase and consequently allows the formation of a re-entrant jet and the cavitation cloud separation. Different values for exponent n were investigated. The most plausible results were obtained with values raging from $n = 7, \ldots, 15$. As recommended by Coutier-Delgosha et al. [19], $n = 10$ was eventually used.

3.4. Mesh and boundary conditions

The computational domain stretched from 10 chord lengths in front of the hydrofoil to 10 chord lengths behind the hydrofoil. The cross sectional dimensions of the domain were the same as the test section dimensions (50 mm wide and 100 mm high). To check the influence of spatial and time discretization, a study of these parameters was made on the basis of comparing the cavity pocket length (Table 1). The discretization error of 0.5% was estimated on the basis of the Richardson extrapolation (Ferziger and Perić [20]). Time step size was more influential. The simulation diverged when time step 10^{-4} s or longer was used. It was determined that at least 100 time steps per shedding period must be used to avoid greater influence. Eventually C-type structured meshes with about 360 000 nodes (Fig. 8) and time step 2×10^{-5} s were used. Standard wall functions were applied; hence the y+ value lies between 30 and 80.

Table 1
Results of spatial and time discretization influence and iteration cut-off influence study (the cavity pocket length is defined as the position of the average 10% vapour volume fraction line measured 5 mm from the front wall at a 1 mm distance from the hydrofoil surface)

Time step (s)	Grid size	Residuals	Shedding frequency (Hz)	Cavity length (mm)
5×10^{-5}	~360 000	5×10^{-4}	251	33
1×10^{-4}	~360 000	5×10^{-4}	Divergence	Divergence
2×10^{-5}	~180 000	5×10^{-4}	276	29
2×10^{-5}	~360 000	5×10^{-4}	262	35
2×10^{-5}	~720 000	5×10^{-4}	253	36
2×10^{-5}	~360 000	1×10^{-3}	259	34
2×10^{-5}	~360 000	5×10^{-5}	263	35

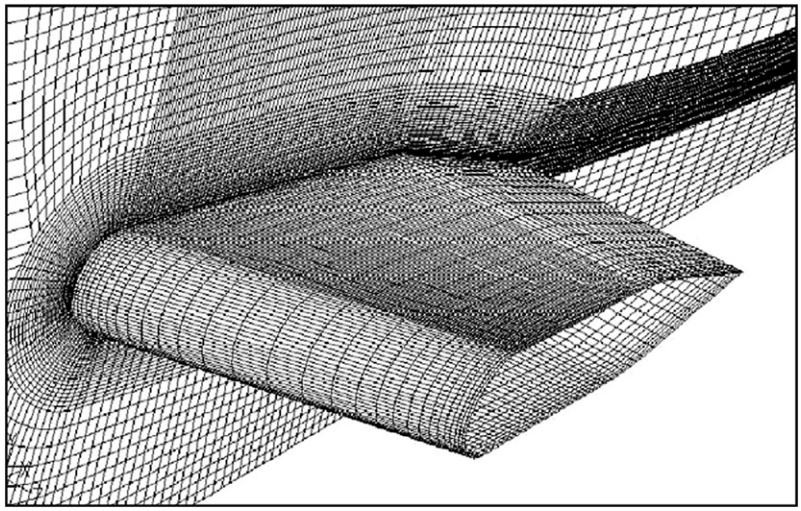

Fig. 8. Computational domain around the hydrofoil.

The convergence criterion was determined by observing the evolution of different flow parameters (velocity magnitude at outlet, static pressure behind the hydrofoil) in the computational domain. The monitored flow parameters were always converged after the sum of the imbalance of the transport equations between iterations over all cells in the computational domain (residuals of the variables: pressure, velocity, turbulent kinetic energy, dissipation of turbulent kinetic energy and volume fraction) fell below 10^{-3} (after the error residuals drop by 3 orders of magnitude). After that, a number of different values (from 10^{-3} to 5×10^{-5}) for residuals were tested, but no significant difference in the solution was found (Table 1). Eventually a criterion for the converged time step solution was set to the point when the residuals fell below 5×10^{-4}. Approximately 40 iterations per time step were needed to obtain a converged solution.

Conditions applied for the simulation were the following:

- Boundary condition: Imposed velocity at inlet and static pressure at outlet. The channel walls were also considered so that the possible wall effects were taken into account.
- Initial transient treatment: A low velocity was initially applied to the flow field, for which no vapour appeared. The velocity was then increased until the desired operating point (cavitation number $\sigma = 2.3$ at flow velocity $v = 13$ m/s) was reached. The turbulence level at inlet boundary condition was set to 3%.
- Because the experimental cavitation number is based on upstream pressure, the losses generated in the test section had to be taken into account in the calculation of the numerical cavitation number. The desired operating point (cavitation number) was reached by comparison of the experimental and numerical upstream pressure. Since the pressure is imposed at the outlet it can slightly oscillate at the inlet into the domain, hence the pressure used to calculate the numerical upstream cavitation number was time averaged. The upstream cavitation number was the same for the experiments and for the simulation (defined at the same point in the domain (5 chord lengths upstream of the hydrofoil); $\sigma = 2.3$). The turbulence level at outlet boundary condition was set to 3%.
- Different time step values were tested; eventually time step 2×10^{-5} s was used (Table 1).
- Hydrofoil incidence angle was 5°.

The values $\rho_l = 998.2$ kg/m^3, $\rho_v = 0.554$ kg/m^3, $\mu_l = 10^{-3}$ Pa s, $\mu_v = 1.34 \times 10^{-5}$ Pa s, $\gamma = 0.0717$ N/m for liquid and vapour density, liquid and vapour dynamical viscosity and liquid surface tension, respectively, were used for the simulation. The gas content of the water was measured during the experiments and the value was given as an input into the simulation ($f_g = 5 \times 10^{-5}$).

A more detailed description of the numerical simulation and additional information on the mesh independence study, boundary conditions and evaluation of the simulation can be found in the previous paper by the present authors (Dular et al. [9]).

4. Simulation results

The transition of the simulated cavitation structures is presented in Fig. 9.

A sequence of images of numerical simulation of cavitation around the hydrofoil is presented. Isosurfaces of 10% vapour volume fractions are shown (the value of 10% vapour volume fraction was chosen on the basis of previous experience that shows that it relates best to the real cavity shapes) (Okita and Kajishima [21]). The time delay between the images is 0.6 ms. As in the experiment (Fig. 1) a steady attached cavitation can be seen in the region where the hydrofoil is the longest. The cloud separation occurs only in the region where the hydrofoil is the shortest. The cavitation structure firstly grows. The re-entrant jet (not presented in the sequence) causes the cavitation cloud separation in the region near the front wall. The separated cloud travels with the flow and implodes downstream in a higher-pressure region. The implosion of the cloud forms a new re-entrant jet that causes the next cavitation cloud separation.

The numerically predicted cavitation cloud frequency was deducted from observation of 15 shedding cycles. It is 262 Hz and varies in the range of about ± 40 Hz from the mean value. The experimental frequency was determined with a high speed CCD camera (3600 fps). The measured frequency is 330 ± 62 Hz (Bachert [15]). Although the simulation predicts lower shedding rate we still consider it to be within the plausible range.

A sequence that shows prediction of instantaneous velocity fields during cavitation cloud separation period on a plane 1 mm above the hydrofoil surface is presented in Fig. 10. The flow is from top to bottom. Both the velocity field and the shape of the cavitation structure are presented. The time delay between the images is 1.2 ms.

It can be seen that the swept leading edge significantly influences the shape of the cavity, which acts on the flow field and violently disturbs it. We can actually see two cloud separations in the sequence. First a small (picture 2) and later a larger cloud (picture 5) separates from the attached part of the cavity. It is interesting to observe the circulation of the flow that is generated by the re-entrant jet. First the re-entrant jet is deviated to the region where the hydrofoil is the shortest (picture 1). The flow then starts to circulate in side the attached cavity and reaches the other side of the hydrofoil (pictures 2–5). It then losses momentum what results in cavitation cloud separation (picture 6). The process then repeats as the re-entrant is deflected to the region where the hydrofoil is the shortest what causes a new circulation of the flow inside the attached cavity. The deviation in the direction of the re-entrant jet can obviously be seen although it seems not to be as intense as Duttweiler and Brennen [2] estimated (Fig. 3). The flow in the region of cloud separation (in the region near the right channel wall) is very disturbed and clear estimates of the direction and the magnitude of the velocity are rather hard to give. For a better comparison an averaged flow field was also evaluated.

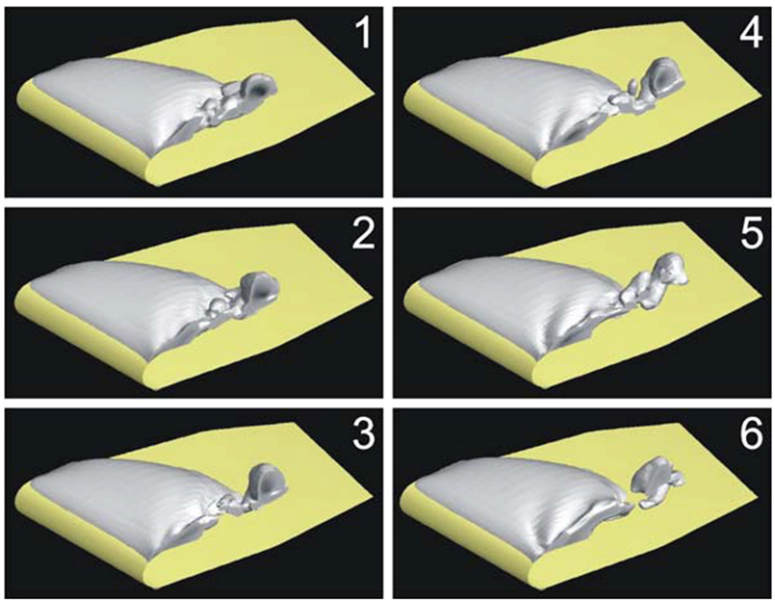

Fig. 9. Numerically predicted time evolution of cavitation structure.

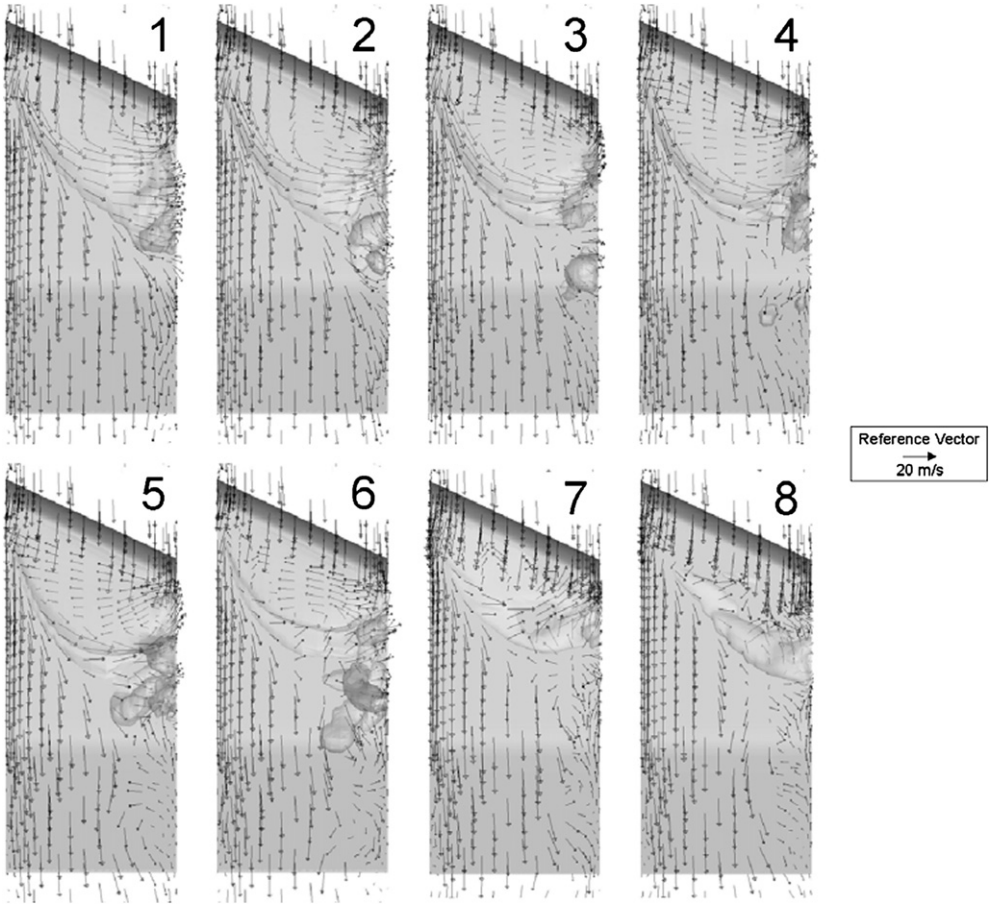

Fig. 10. Numerically predicted sequence of instantaneous velocity fields with corresponding cavitation structures.

In all a period 0.1 s long (about 30 periods of cavitation cloud shedding) was simulated. The data from all time steps was averaged to acquire an average flow field condition. The convergence study revealed that the uncertainty of the magnitude of mean velocity and mean cavitation structure shape is less than 1% when all the data was averaged (Dular et al. [9]).

Fig. 11 presents contour diagrams of mean x (left) and y velocity (right) magnitude.

While the x-velocity component represents the flow in the incipient flow direction (from the top to the bottom in Fig. 11), the y-velocity component gives the flow velocity perpendicular to the incipient flow (from the left to the right in Fig. 11). The flow is undisturbed as it approaches the hydrofoil (velocity is homogeneous at $v_x \approx 13$ m/s and $v_y \approx 0$ m/s). As it passes the leading edge of the hydrofoil the velocity magnitude increases and a slight deviation to the right side (looking in the main flow direction; to left side in the diagram) can be seen. Further on (already inside and downstream of the cavitation pocket) a clear deviation to the left side (looking in the main flow direction; to right side in the diagram) – to the region where the hydrofoil is the shortest, can be seen from y-velocity diagram in Fig. 11. The y-velocity component increases up to $v_y \approx 5$ m/s. A significant backflow can also be seen from the x-velocity diagram. In the region where the hydrofoil is the shortest a region with negative x-velocity component exists (up to $v_x \approx -5$ m/s). Since this region is present only in the vicinity of the right wall (looking at Fig. 11) and not over the whole span of the hydrofoil (as one would expect if the swept leading edge would have no effect on the direction of the re-entrant jet), we can confidently say that the re-entrant jet indeed gains the velocity in the y direction and is therefore deviated to this region where it causes cavitation cloud separation.

In Fig. 12 an average velocity field (vectorplot) with noted mean cavitation structure shape is presented. The mean shape of the cavitation structure was determined by averaging the 10% vapour volume fraction contour on the plane 1 mm above the hydrofoil surface.

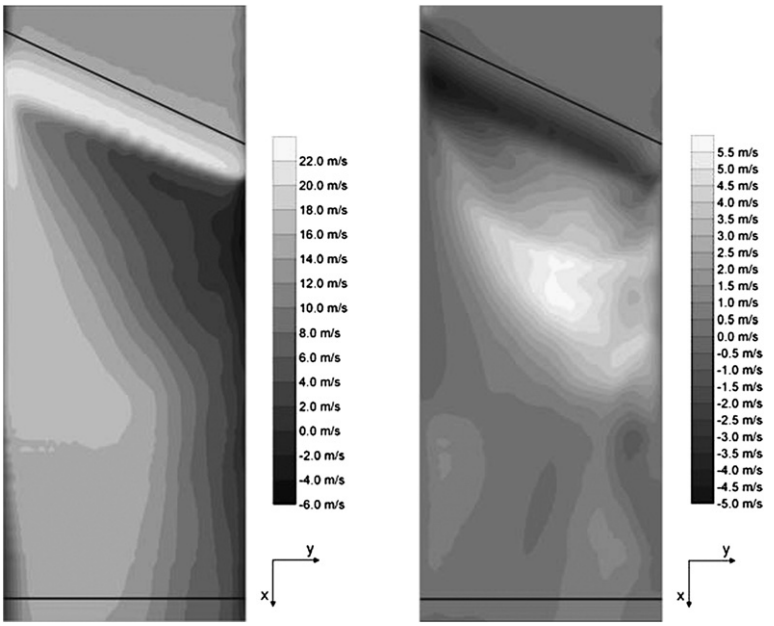

Fig. 11. Numerically predicted mean x and y velocity distributions.

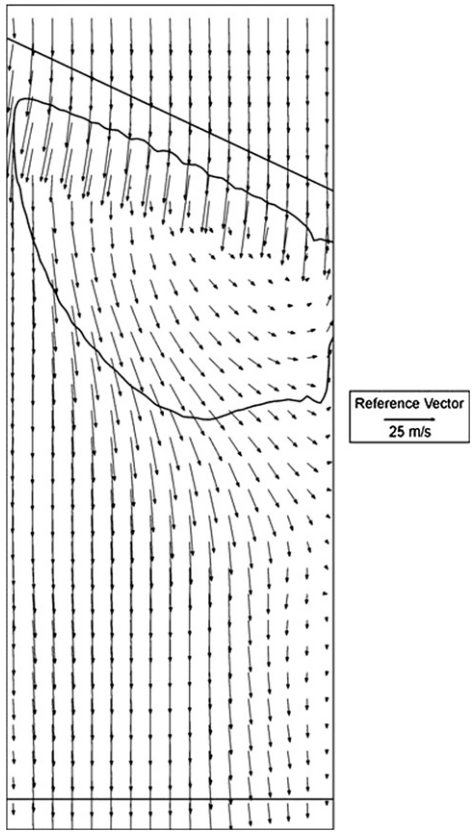

Fig. 12. Numerically predicted velocity field (vector-plot) with noted mean cavity shape.

The resemblance of the simulation results and the hypothesis by Duttweiler and Brennen [2] is obvious (Figs. 3 and 12), although the deviation of the flow is not as pronounced as the hypothesis suggested. The main reason for the discrepancy probably lies in the fact that the authors of the hypothesis presumed a zero pressure gradient at the cavity closure line, which is in fact wrong. The small pressure gradient in this region decreases the velocity in the direction tangential to the cavity closure line, what consequently results in a smaller deviation of the re-entrant jet.

The undisturbed flow deviates to the right side (looking in the direction of the flow; to the left side in the diagram) as it just passes the leading edge of the hydrofoil. In the region where the hydrofoil is the shortest a very clear indication of the re-entrant jet can be seen. Near the cavitation pocket begin, both the flow in the positive and negative x direction (main flow direction) are present. This high vorticity implies that the cavitation cloud will separate there, what was also observed during experiment (Fig. 1) and simulation (Fig. 9).

Results gained by the numerical simulation imply that the hypothesis (Figs. 2 and 3) that was purposed by de Lange and de Bruin [1] and Duttweiler and Brennen [2] is correct, but still an experimental proof is needed to fully accept the idea.

5. Experimental evaluation of the flow

For noncavitating flow at high cavitation numbers (upstream pressure $p_\infty = 5.1$ bar, $v = 13$ m/s; $\sigma = 6$) a purely two-dimensional flow without separation can be observed. Fig. 13 shows an instantaneous velocity field on a plane 1 mm above the hydrofoil surface at noncavitating conditions.

One can see that flow does not deviate significantly from the mean flow direction. The only clear deviation can be seen at the transition from the curved to the plane part of the hydrofoil, which is caused by the small difference in pressures on the channel walls. As it was presented in the previous paper from the present authors (Dular et al. [9]) the

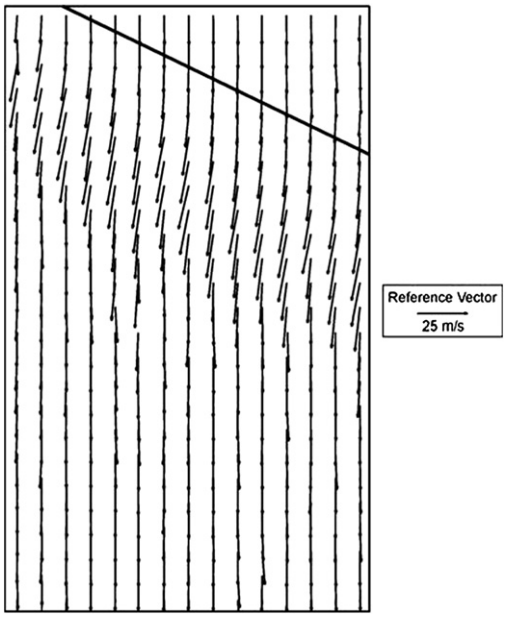

Fig. 13. Instantaneous velocity field above a noncavitating hydrofoil.

flow separation also does not occur in the plane perpendicular to the hydrofoil surface. It can be therefore expected that the main mechanism for the asymmetric cavitation cloud separation is in fact the re-entrant jet deflection at the cavity closure line.

Observations by Bachert [15] show that cavitation inception occurs at $\sigma = 3.6$. It first appears in the region where the hydrofoil is the shortest and expands over the whole width of the hydrofoil as the cavitation number is decreased – this occurs approximately at $\sigma = 3.0$. At $\sigma = 2.7$ small cavitation clouds begin to shed in the region where the hydrofoil is the shortest.

Fig. 14 shows a probable sequence of cavitation cloud separation. It was constructed from single PIV-LIF and cavitation image data sets by comparing them to the sequence of cavitation cloud separation recorded by the high speed camera (Bachert [15]). Although we cannot say for sure that the images follow the correct order of events a resemblance to the numerically predicted sequence (Fig. 10) can obviously be seen. Cavitation structures with corresponding velocity fields can be seen (the colours are inverted). The flow is from top to bottom.

Picture 1 in Fig. 14 shows the situation just before the cloud separates. One can see that an attached cavitation pocket exists over the whole span of the hydrofoil. Also no separated cavitation cloud can be seen downstream of the attached pocket. If the velocity field is observed a clear vortex can be seen in the region where the hydrofoil is the shortest. In the spanwise direction the vorticity extends from the right channel wall (where flow in the upstream direction can be seen) to about 35% of the whole span of the hydrofoil. In the next situation (picture 2) a cloud begins to separate. A separated "horseshoe" shaped cavitation cloud can be seen in the immediate vicinity downstream of the attached cavity in the region where the hydrofoil is the shortest. The region where the vortex is present extends to about 55% of the span of the hydrofoil. The situation is similar to what the simulation predicted (Fig. 10) where the re-entrant jet begins to travel towards the left channel wall. Picture 3 shows that the separated cavitation cloud moved further downstream and that the vortex (re-entrant jet) progressed further towards the part where the hydrofoil is the longest (to about 65% of the hydrofoil span) but it is slowly loosing momentum since the spanwise velocities are decreasing. The loss of momentum can be again seen in picture 4 where the vortex decreases to about 55% of the span of the hydrofoil. Meanwhile the, still horseshoe shaped, cavitation cloud travels downstream with the flow. The cloud can hardly be seen further on downstream in picture 5 as it is just before the collapse. The vortex looses its momentum and decreases to about 40% of the hydrofoil span. In the last picture of the sequence again only the attached cavity can be seen and a vortex about 30% of the hydrofoil span big can be observed. After that the process will start again as the vortex will grow and the next cavitation cloud will separate.

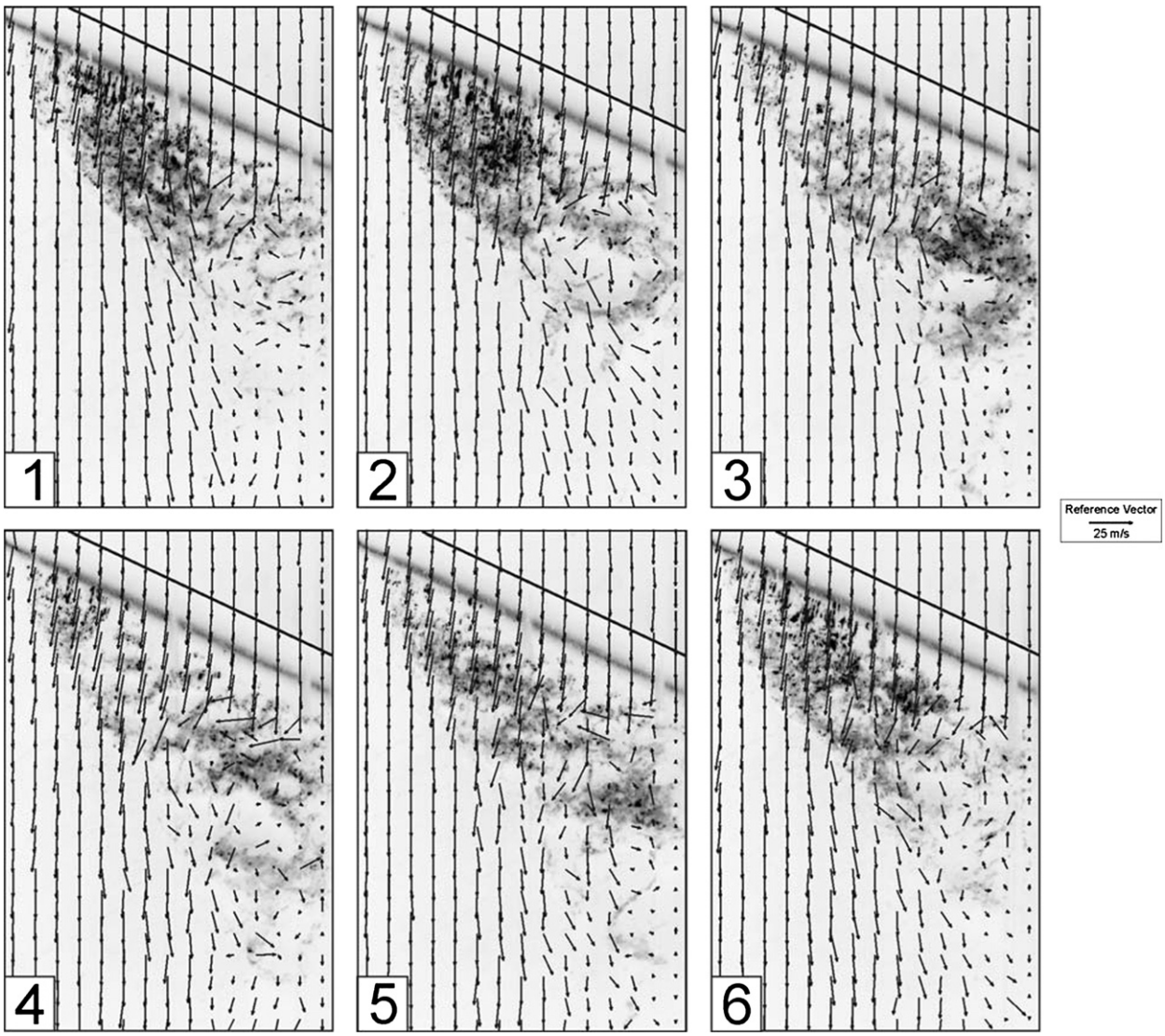

Fig. 14. Probable sequence of measured instantaneous velocity fields with corresponding cavitation structures.

To enable a clear evaluation mean velocity fields were determined by averaging 50 instantaneous PIV-LIV data sets (the convergence study by Dular et al. [9] revealed that the uncertainty of the magnitude of mean velocity is less than 1.5% when more than 40 data sets are averaged).

Fig. 15 shows measured average x and y velocities on a plane 1 mm above the hydrofoil surface.

The flow seems to be undisturbed as it approaches the hydrofoil – $v_x \approx 13$ m/s and $v_y \approx 0$ m/s. Measurements confirm that it deviates slightly to the region where the hydrofoil is the longest as it passes the transition from the circular to the plane part of the hydrofoil. This can be related to the small pressure difference that occurs as a result of quicker acceleration of the flow in the region where the hydrofoil is the longest. Downstream (in the region where cavitation cloud separations occur) the flow begins to deviate toward the other wall – the y-velocity increases from approximately $v_y \approx -1$ m/s to about $v_y \approx 5$ m/s. Also in this region (especially near the channel wall) negative x-velocities ($v_x \approx -5$ m/s) can be seen. The measured results and the results of numerical simulation correlate very well. They also both resemble predictions that were purposed by de Lange and de Bruin [1] and Duttweiler and Brennen [2] so we can again say that their hypothesis seems plausible.

To further support the interpretation of the results the average measured velocity field in a form of a vectorplot with corresponding average cavitation structure on a plane 1 mm above the hydrofoil surface is presented in Fig. 16.

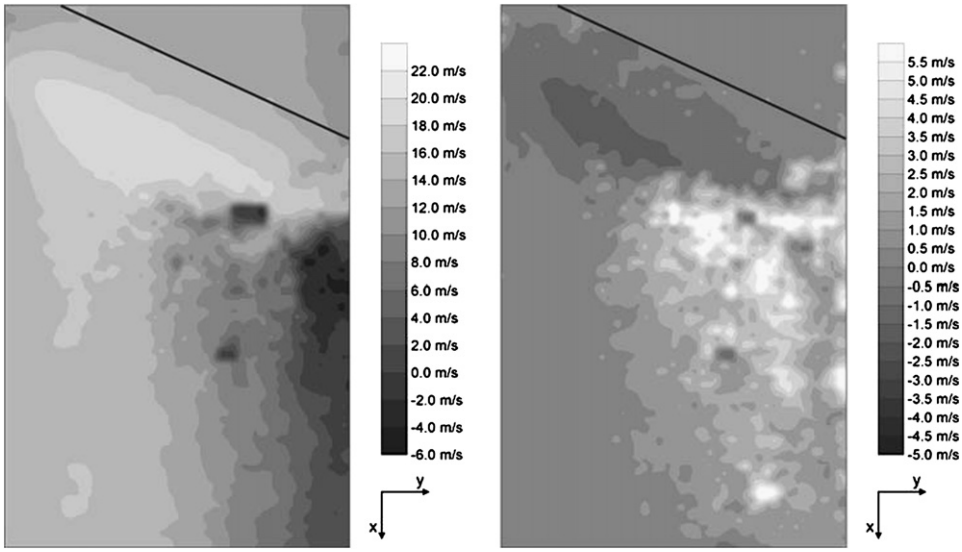

Fig. 15. Measured x and y velocity distributions.

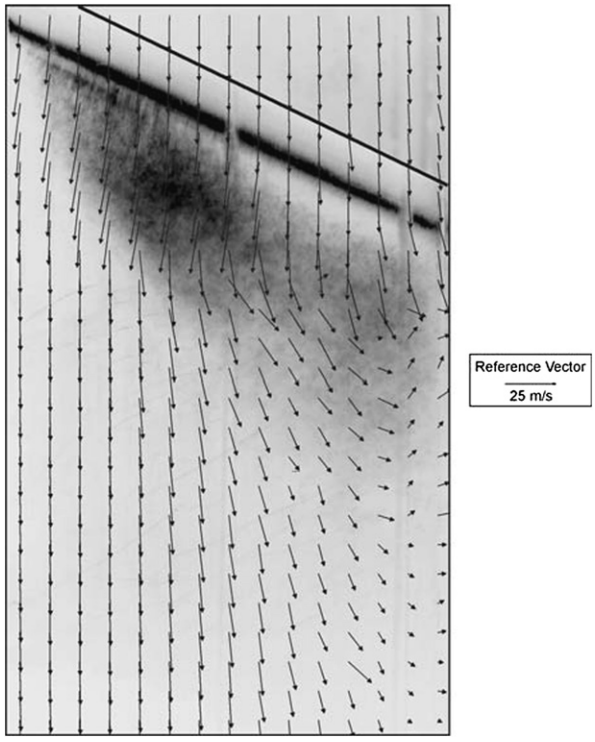

Fig. 16. Measured average velocity field (vectorplot) with noted average cavitation structure shape.

Very similarly to the simulation results (Fig. 12), results of PIV-LIF measurements obviously resemble the prediction by Duttweiler and Brennen [2] (Fig. 3), but again the deviation of the flow is not as specific as they assumed (as already stated the reason probably lies in the fact that they assumed a nonzero pressure gradient at the cavity closure line).

The flow deviates to the region where the hydrofoil is the shortest approximately from the middle of the span (width) of the hydrofoil. Negative x-velocities (re-entrant jet), however, exist only in a very thin region near the

channel wall (better seen in the left diagram in Fig. 15), which is consequently also the region where cavitation clouds separate.

Again we can conclude, on the basis of experimental measurements, that the hypothesis (Figs. 2 and 3) that was purposed by de Lange and de Bruin [1] and Duttweiler and Brennen [2] is correct, but has a small aesthetic error since they predicted a more pronounced flow deviation.

6. Conclusions

The influence of the swept leading edge on the behaviour of the cavitation is well known. The most plausible explanation for the asymmetric cavitation cloud separation was proposed by de Lange and de Bruin [1] and Duttweiler and Brennen [2]. They suggested that the re-entrant jet velocity gains a spanwise component if the closure line of the cavity is inclined. Their explanation, however, lacked an experimental or at least numerical proof, since it was based only on visual observation of the behaviour of cavitation structures.

In the present paper first an unsteady simulation of cavitating flow is presented. The capability of the numerical simulation to predict different characteristics of cavitating flow was studied previously by the present authors (Dular et al. [9]). In the present paper results of numerically predicted instantaneous and average velocity fields were presented. They all imply that the hypothesis made by de Lange and de Bruin [1] and Duttweiler and Brennen [2] is correct, although the flow deviation is not as pronounced as suggested. Further on an experimental investigation of the phenomenon was pursued. A relatively new experimental technique where PIV method is combined with LIF method was used for the determination of the velocity field on a plane 1 mm above the cavitating hydrofoil surface. The use of additional camera made it possible to determine the instantaneous cavitation structure shape and the corresponding velocity field inside and outside the cavitation structure. Like previously numerical simulation, results of measurements proved that the hypothesis purposed by de Lange and de Bruin [1] and Duttweiler and Brennen [2] generally "holds water".

References

[1] D.F. de Lange, G.J. de Bruin, Sheet cavitation and cloud cavitation, re-entrant jet and three-dimensionality, Applied Scientific Research 58 (1998) 91–114.
[2] M.E. Duttweiler, C.E. Brennen, Partial cavity instabilities, in: Proc. of US-Japan Seminar: Abnormal Flow Phenomena in Turbomachines, Osaka, Japan, November 1–6, 1998.
[3] K.R. Laberteaux, S.L. Ceccio, Partial cavity flows. Part 2. Cavities forming on test objects with spanwise variation, Journal of Fluid Mechanics 431 (2001) 43–63.
[4] A. Kubota, K. Hiroharu, H. Yamaguchi, A new modelling of cavitating flows, a numerical study of unsteady cavitation on a hydrofoil section, Journal of Fluid Mechanics 240 (1992) 59–96.
[5] R. Kunz, D. Boger, D. Stinebring, T. Chyczewski, J.W. Lindau, H.J. Gibeling, S. Venkateswaran, T.R. Govindan, A preconditioned implicit method for two-phase flows with application to cavitation prediction, Computers and Fluids 29 (8) (2000) 849–875.
[6] I. Senocak, I.W. Shyy, A pressure-based method for turbulent cavitating flow simulations, Journal of Computational Physics 176 (2002) 363–383.
[7] A.K. Singhal, H. Li, M.M. Atahavale, Y. Jiang, Mathematical basis and validation of the full cavitation model, Journal of Fluids Engineering 124 (2002) 617–624.
[8] F.M. Owis, A.H. Nayfeh, Numerical simulation of 3-D incompressible, multi-phase flows over cavitating projectiles, European Journal of Mechanics B Fluids 23 (2004) 339–351.
[9] M. Dular, R. Bachert, B. Stoffel, B. Širok, Experimental evaluation of numerical simulation of cavitating flow around hydrofoil, European Journal of Mechanics B Fluids 24 (4) (2005) 522–538.
[10] Y. Zhang, S. Gopalan, J. Katz, On the flow structure and turbulence in the closure region of attached cavitation, in: 22nd ONR Symp. on Naval Hydrodynamics, 1998, pp. 227–238.
[11] R. Bachert, B. Stoffel, R. Schilling, M. Frobenius, Three-dimensional, unsteady cavitation effects on a single hydrofoil and in a radial pump – measurements and numerical simulations; Part one: experiments, in: Proceedings of the Fifth International Symposium on Cavitation, Osaka, Japan, 2003.
[12] J. Friedrichs, G. Kosyna, Unsteady PIV flow field analysis of a centrifugal pump impeller under rotating cavitation, in: Proceedings of the Fifth International Symposium on Cavitation, Osaka, Japan, 2003.
[13] M. Hofmann, H. Lohrberg, G. Ludwig, B. Stoffel, J.L. Reboud, R. Fortes-Patella, Numerical and experimental investigations on the self-oscillating behaviour of cloud cavitation – Part 1: Visualisation, in: Proceedings of the 3rd ASME / JSME Joint Fluids Engineering Conference, San Francisco, CA, 1999.
[14] Y. Iwai, S. Li, Cavitation erosion in waters having different surface tensions, Wear 254 (2003) 1–9.

[15] R. Bachert, Dreidimensionale, instationaere Effekte kavitierender Stroemungen – Analyse an Einzelproffilen und in einer Radialpumpe, PhD work, Darmstadt University of Technology, Darmstadt, 2004.
[16] S.V. Patankar, Numerical Heat and Fluid Flow, Hemisphere, New York, 1980.
[17] V. Yakhot, S.A. Orszag, Renormalization-group analysis of turbulence, Physical Review Letters 57 (1986) 1722–1724.
[18] J.L. Reboud, B. Stutz, O. Coutier, Two-phase flow structure of cavitation: experiment and modelling of unsteady effects, in: Third International Symposium on Cavitation, Grenoble, France, 1998.
[19] O. Coutier-Delgosha, R. Fortes-Patella, J.L. Reboud, Evaluation of turbulence model influence on the numerical simulations on unsteady cavitation, Journal of Fluids Engineering 125 (2003) 38–45.
[20] J.H. Ferziger, M. Perić, Computational Methods for Fluid Dynamics, second ed., Springer, 1999.
[21] K. Okita, T. Kajishima, Three-dimensional computation of unsteady cavitating flow in a cascade, in: The 9th of International Symposium on Transport Phenomena and Dynamics of Rotating Machinery, Honolulu, Hawaii, 2002.